Editors' Suggestion

Observation of Topological *p*-Orbital Disclination States in Non-Euclidean Acoustic Metamaterials

Ying Chen,[1,*,†] Yuhang Yin,[2,*] Zhi-Kang Lin,[3,*] Ze-Huan Zheng,[2] Yang Liu,[3] Jing Li,[2] Jian-Hua Jiang,[3,‡] and Huanyang Chen[2,§]

[1]*Department of Physics, College of Information Science and Engineering, Huaqiao University, Xiamen 361021, China*
[2]*Department of Physics and Pen-Tung Sah Institute of Micro-Nano Science, Xiamen University, Xiamen 361005, China*
[3]*Institute of Theoretical and Applied Physics, School of Physical Science and Technology, and Collaborative Innovation Center of Suzhou Nano Science and Technology, Soochow University, 1 Shizi Street, Suzhou 215006, China*

(Received 13 February 2022; accepted 6 September 2022; published 3 October 2022)

Disclinations—topological defects ubiquitously existing in various materials—can reveal the intrinsic band topology of the hosting material through the bulk-disclination correspondence. In low-dimensional materials and nanostructure such as graphene and fullerenes, disclinations yield curved surfaces and emergent non-Euclidean geometries that are crucial in understanding the properties of these materials. However, the bulk-disclination correspondence has never been studied in non-Euclidean geometry, nor in systems with *p*-orbital physics. Here, by creating *p*-orbital topological acoustic metamaterials with disclination-induced conic and hyperbolic surfaces, we demonstrate the rich emergent bound states arising from the interplay among the real-space geometry, the bulk band topology, and the *p*-orbital physics. This phenomenon is confirmed by clear experimental evidence that is consistent with theory and simulations. Our experiment paves the way toward topological phenomena in non-Euclidean geometries and will stimulate interesting research on, e.g., topological phenomena for electrons in nanomaterials with curved surfaces.

DOI: 10.1103/PhysRevLett.129.154301

Despite their abundance in various materials, topological defects [1–5] (such as disclinations and dislocations) have been studied limitedly in topological physics [6–18]. Only recently, topological defects were used as unique experimental probes of topological phases [19–31]. For instance, in topological crystalline insulators, bulk-disclination correspondence was found to connect the bulk band topology to the fractional charges and local modes bound to disclinations, providing more information on bulk topology than the conventional bulk-edge correspondence [22,23]. In weak topological insulators [21,24,25] and topological crystalline insulators [26], helical 1D modes induced by screw dislocations were observed. These studies unveil a regime where the interplay between the band topology in momentum space and the real-space topology of defects plays a central role—a field where both theory and experiments are underdeveloped.

In particular, to date, the few experimental studies on disclinations focus only on planar (Euclidean) geometries [22,23,28–30], whereas nonplanar (non-Euclidean) geometries remain unexplored, although disclinations in low-dimensional materials and nanostructures often lead to deformed surfaces and hence non-Euclidean geometries [32] (see the case of graphene in Refs. [2–5,33–35]). The abundant geometries induced by topological defects in low-dimensional materials and nanostructures offer a versatile platform to study topological phenomena for electrons and phonons which is a realm yet to be investigated. Moreover, the existing studies on topological defects are based mainly on *s*-orbital-like models, while higher-orbital physics, which has been revealed to yield rich emergent phenomena [36–40] and to be relevant for phonons and elastic waves [31,41] in various materials, is rarely explored.

Here, we fill these gaps by studying the topological modes bound to disclinations with conic and hyperbolic surfaces in a *p*-orbital valley Hall acoustic metamaterial. Neither conic or hyperbolic structure nor *p*-orbital topological valley Hall insulators have been studied in acoustic metamaterials. Here, by creating the *p*-orbital valley Hall acoustic metamaterial, we study the acoustic analog of topological phenomena induced by disclinations on curved (non-Euclidean) surfaces. We find that the coexisting non-Euclidean geometries in real space and the topological acoustic bands in reciprocal space yield emergent topological modes bound to disclinations. The topological modes are observed via acoustic pump-probe measurements, revealing rich *p*-orbital wave patterns depending on the disclination geometries. The consistent theory, simulations, and experiments confirm the underlying bulk-defect physics which would inspire future studies on topological phenomena of electrons and phonons on curved surfaces.

We start from a 2D honeycomb lattice with *A*- and *B*-type sites [Fig. 1(a)]. Non-Euclidean disclinations can be constructed through the cut-and-glue procedures: By

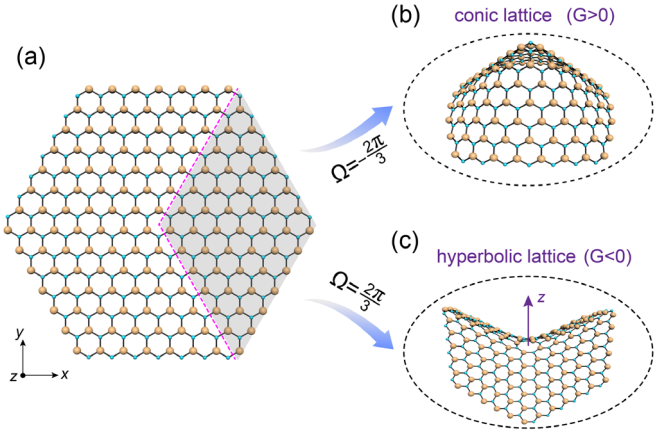

FIG. 1. (a) A 2D honeycomb lattice consists of the A-type (yellow) and B-type (blue) sublattice sites. The shaded region denotes a $2\pi/3$ sector (enclosed by the magenta dashed lines). (b) and (c) Schematics of the conic (hyperbolic) lattice constructed by removing (adding) a $2\pi/3$ sector from (into) the honeycomb lattice, leading to a disclination with the Frank angle $\Omega = -(2\pi/3)$ $(2\pi/3)$. G represents the Gaussian curvature of the structure.

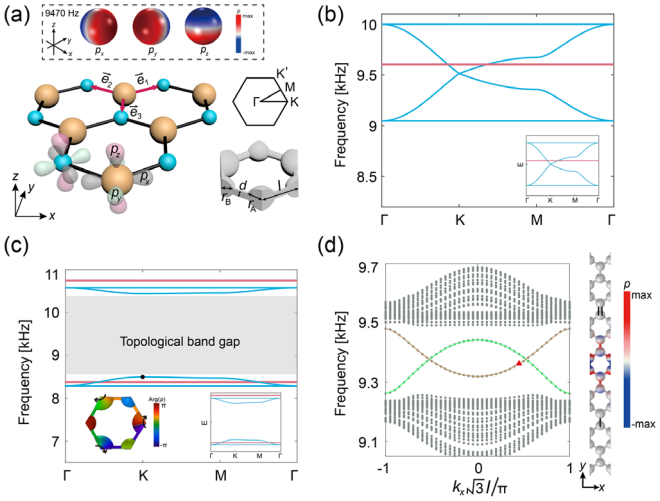

FIG. 2. (a) Honeycomb lattice with acoustic p orbitals (top panel; also depicted in the main panel). $\vec{e}_1$, $\vec{e}_2$, and $\vec{e}_3$ denote three hopping vectors. Upper right: the Brillouin zone. Lower right: a unit cell of the acoustic metamaterial (gray denotes air regions) with geometric details. (b) and (c) Simulated band structures of acoustic metamaterials with different parameters: (b) $r_A = r_B = 12$ mm, (c) $r_A = 13.5$ mm and $r_B = 10.5$ mm. Cyan curves represent the p_x and p_y bands, while red curves denote the p_z bands. Insets: band structures from the tight-binding model: (b) $\varepsilon_{Ax,y} = \varepsilon_{Bx,y} = 0$, $\varepsilon_{Az} = \varepsilon_{Bz} = 0.3$, (c) $\varepsilon_{Ax,y} = -1.8$, $\varepsilon_{Az} = -2.1$ and $\varepsilon_{Bx,y} = 2$, $\varepsilon_{Bz} = 2.8$. In panel (c), acoustic phase profile (arrows indicate the phase winding) at the K point (black dot) is also depicted. (d) Dispersions for a supercell with zigzag edge boundaries between two acoustic metamaterials I and II. The radii are $r_A = 12.3$ mm and $r_B = 11.7$ mm for I (r_A and r_B are interchanged for II), respectively. Right: acoustic pressure profile for the edge state at the red triangle in the brown curve. Green curve is for the edge states at the opposite edge. $l = 31.0$ mm and $d = 5.6$ mm.

removing or inserting a $2\pi/3$ sector of the lattice, a conic or saddle surface can be constructed through the Kamada-Kawai layout algorithm [42]. This algorithm provides the minimal deformation of the local lattice geometry even when the Frank angle is large. The resultant structure exhibits either a positive ($G > 0$, conic lattice) or negative ($G < 0$, hyperbolic lattice) Gaussian curvature [Figs. 1(b) and 1(c)] [43]. Such curved surfaces, which are common in low-dimensional and nanomaterials [33], are natural consequences of disclinations due to minimization of the deformation energy. Here, we show that they play an important role in the emergence of the disclination states.

We consider spherical acoustic cavities that each support three degenerate acoustic modes, the p_x, p_y, and p_z orbitals. Placing such cavities on the honeycomb lattice as in Fig. 2(a), a p-orbital acoustic metamaterial is realized. The rich orbital overlapping geometries between the A- and B-type cavities yield two types of couplings [44,45]: the dominant σ-type couplings t_σ and the negligible π-type couplings (see Supplemental Material [46]). Neglecting the latter, the tight-binding Hamiltonian is thus

$$H = \begin{bmatrix} \varepsilon_{Ax} & 0 & 0 & \frac{3t_\sigma}{4}(e^{i\vec{k}\cdot\vec{e}_1} + e^{i\vec{k}\cdot\vec{e}_2}) & \frac{\sqrt{3}t_\sigma}{4}(e^{i\vec{k}\cdot\vec{e}_1} - e^{i\vec{k}\cdot\vec{e}_2}) & 0 \\ 0 & \varepsilon_{Ay} & 0 & \frac{\sqrt{3}t_\sigma}{4}(e^{i\vec{k}\cdot\vec{e}_1} - e^{i\vec{k}\cdot\vec{e}_2}) & \frac{t_\sigma}{4}(e^{i\vec{k}\cdot\vec{e}_1} + e^{i\vec{k}\cdot\vec{e}_2}) + t_\sigma e^{i\vec{k}\cdot\vec{e}_3} & 0 \\ 0 & 0 & \varepsilon_{Az} & 0 & 0 & 0 \\ & & & \varepsilon_{Bx} & 0 & 0 \\ & \text{H.c.} & & 0 & \varepsilon_{By} & 0 \\ & & & 0 & 0 & \varepsilon_{Bz} \end{bmatrix}, \quad (1)$$

where $\varepsilon_{A\alpha}$ and $\varepsilon_{B\alpha}$ ($\alpha = x, y, z$) denote the onsite energy of the p_α orbital on the A and B sites, respectively. In the off-diagonal terms, $\vec{e}_{1,2} = [\pm(\sqrt{3}/2), \frac{1}{2}]$ and $\vec{e}_3 = (0, -1)$ are the nearest-neighbor hopping vectors, and the prefactors are determined by the p-orbital geometries [45]. The tight-binding Hamiltonian captures the main features of the acoustic bands, as shown in Figs. 2(b) and 2(c). In the acoustic metamaterial, the on-site energy can be controlled

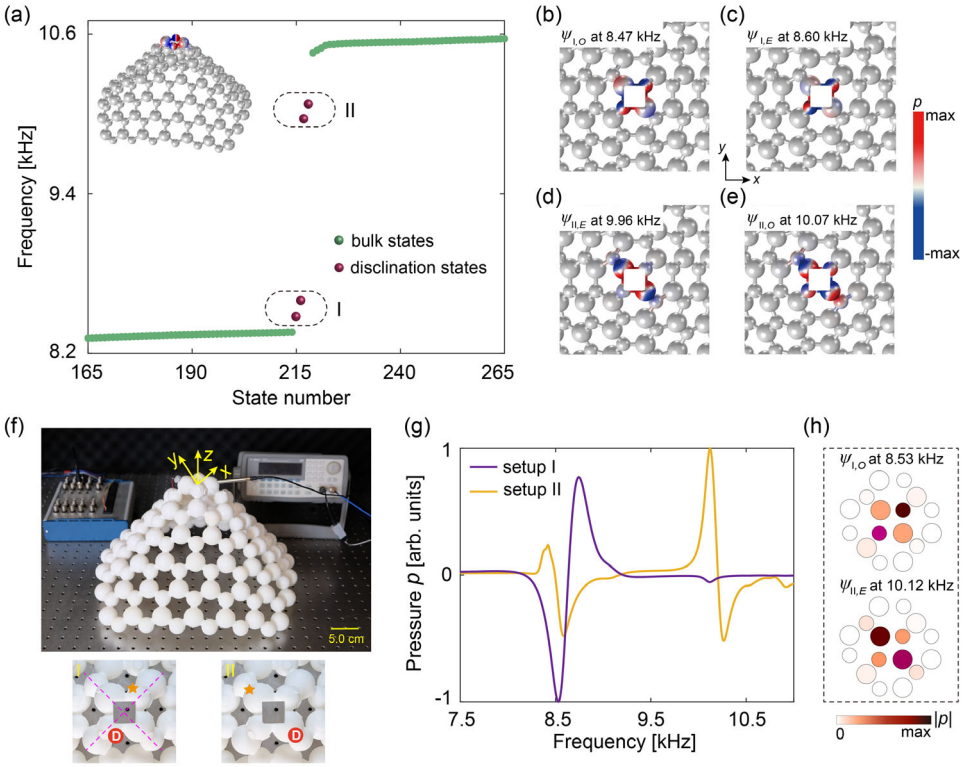

FIG. 3. (a) Simulated acoustic eigenfrequencies around the topological band gap in the conic lattice with $r_A = 13.5$ mm, $r_B = 10.5$ mm, and $d = 5.6$ mm. Topological disclination states in groups I and II are labeled by the purple dots. Inset shows the acoustic pressure profile of a disclination state. (b)–(e) Top views of the simulated acoustic pressure profiles for the disclination states. (f) Photograph of the fabricated acoustic structure for the conic lattice and the experimental setup. In the lower panels, the pump-probe configurations I and II are shown where the stars (dots) denote the positions of the acoustic source (detector). Purple dashed lines indicate the mirror symmetry lines. (g) Measured acoustic pressure p for the pump-probe configurations I and II at different frequencies. (h) Measured acoustic pressure profiles $|p|$ (absolute value) around the disclination core (cavities are depicted as circles) for two disclination states, $\Psi_{\mathrm{I},O}$ and $\Psi_{\mathrm{II},E}$, under resonant excitation conditions.

by the radii r_A and r_B for the cavities at the A and B sites, respectively. When $r_A = r_B = 12$ mm, the acoustic Dirac cones emerge at the K and K' points as derived from the p_x and p_y orbitals [Fig. 2(b)], while the two p_z flat bands are degenerate. By setting $r_A = 13.5$ mm and $r_B = 10.5$ mm, both the Dirac cones and the flat bands are gapped, leading to a topological valley Hall band gap due to inversion symmetry breaking [see Fig. 2(c)]. The phase profile of the acoustic wave [inset of Fig. 2(c)] shows the valley vortex state—a signature of valley Hall insulators [47,48]. To demonstrate the valley Hall effect straightforwardly, we construct a supercell with zigzag edge boundaries in simulation. The obtained acoustic band structure and wave functions [Fig. 2(d)] give notable valley Hall edge states with in-plane p-orbital wave patterns.

We use the symmetry representations of the acoustic bands to describe the band topology [49]. Here, the acoustic metamaterial has the threefold (C_3) rotation symmetry. At a high symmetry point denoted as Π, the C_3 eigenvalue $\Pi_p = e^{2\pi i(p-1)/3}$ $(p = 1, 2, 3)$ can be obtained from simulations (see Supplemental Material [46]). The topological invariants are given by $\chi = ([K_1], [K_2])$ with $[K_p] = \#K_p - \#\Gamma_p$, where $\#K_p$ $(\#\Gamma_p)$ stands for the number of bands below the band gap at the K (Γ) point with the C_3 eigenvalues K_p (Γ_p). The topological invariants for the acoustic band gap in Fig. 2(c) are $\chi = (1, 0)$, which is distinct from previous C_3-symmetric higher-order topological insulators derived from s orbitals [49,50]. This band gap is an acoustic analog of both p-orbital valley Hall insulator and higher-order topological insulator as revealed by the emergence of the valley Hall edge states [Fig. 2(d)] and the corner states (Supplemental Material [46]).

The interplay between the band topology in momentum space and the real-space topology of a disclination gives rise to topological bound modes (denoted as disclination modes) and a fractional mode charge $Q_{\mathrm{dis}} = -(\Omega/2\pi)[K_1]$ mod 1 where Ω is the Frank angle [15]. For the curved surface with $G > 0$ ($G < 0$), the Frank angle is $\Omega = -2\pi/3$ $(2\pi/3)$, yielding a fractional mode charge $Q_{\mathrm{dis}} = 1/3$ $(2/3)$ which is distinct from previous findings [22,23]. For acoustic systems, Q_{dis} should be interpreted as the integration of the local density of states of phonons up to the

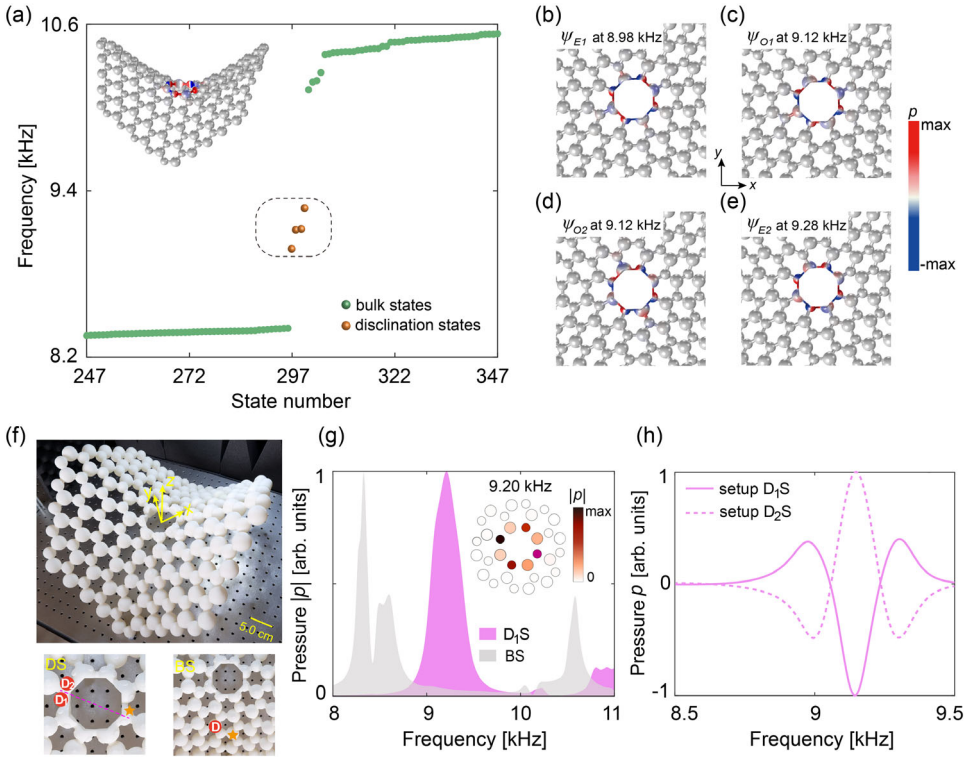

FIG. 4. (a) Simulated acoustic eigenfrequencies around the topological band gap in the hyperbolic lattice with $r_A = 13.5$ mm, $r_B = 10.5$ mm, and $d = 5.6$ mm. Topological disclination states are labeled by the golden dots. Inset shows the acoustic pressure profile of a disclination state. (b)–(e) Top views of the acoustic pressure profiles of the disclination states. (f) Photograph of the fabricated acoustic structure for the hyperbolic lattice. Lower panels show the disclination and bulk pump-probe setups (labeled as DS and BS, respectively) where the stars (dots) denote the positions of the acoustic source (detector). (g) Measured acoustic pressure $|p|$ (absolute value) for the disclination and bulk pump-probe setups versus the excitation frequency. Inset gives the measured acoustic pressure profile for the cavities (depicted as circles) around the disclination core at the excitation frequency of 9.20 kHz. (h) Measured responses for the D_1S and D_2S pump-probe setups.

band gap [24]. A simple interpretation of the above phenomena is based on the Wannier orbitals. There are three p-type Wannier orbitals at the A-type sites [46]. As the disclination boundary runs through the Wannier centers, it induces boundary modes as well as charge separation and fractionalization at the disclination core, similar to the mechanism revealed in Ref. [24] (see Supplemental Material [46] for more details).

We fabricate a conic acoustic metamaterial with 144 cavities. We find from simulations that four disclination states emerge in the band gap [divided into groups I and II in Fig. 3(a)]. The conic lattice has an emergent C_2 rotation symmetry. Hence the disclination states have either even or odd parity and show rich patterns of in-plane p orbitals [Figs. 3(b)–3(e)]. Additionally, for the disclination states in group I (II), the waves are mainly localized in B-type (A-type) cavities and exhibit π-like (σ-like) bonding.

To observe these properties in experiments, we fabricate the acoustic metamaterial via 3D printing technology based on epoxy and use pump-probe techniques to detect the disclination states. As shown in Fig. 3(f), to measure the acoustic signals inside the cavity, holes with a diameter of 8 mm are left on each excitation and detection cavity, and we keep the holes in all other cavities (except for the source and detection position) closed by plastic plugs when measuring the acoustic fields in experiments. An acoustic source (a tiny speaker) is placed into the excitation cavity, which is connected to a waveform generator to launch the broadband acoustic signals, meanwhile, a probe microphone is put into another cavity to detect the acoustic signal there. The detected signal, which reflects the acoustic pressure, is recorded by a DAQ card (NI USB-6361). Through the Fourier transformation of the detected time-dependent acoustic signal, we can obtain the pump-probe responses in the frequency domain (see Supplemental Material [46] for details) which are used to analyze the disclination states here.

According to the wave patterns of the disclination states, a pump-probe configuration with the source and detectors in the B-type (A-type) cavities [denoted as I (II) in the inset of Fig. 3(f)] is used to detect the disclination modes in groups I (II). For pump-probe I, we observe a dip (peak) at 8.53 (8.74) kHz [Fig. 3(g)]. This dip (peak) is associated with the disclination state $\Psi_{I,O}$ ($\Psi_{I,E}$), which appears because $\Psi_{I,O}$ ($\Psi_{I,E}$) overlaps with the source and detector with the opposite (same) wave amplitude. Thus, the

measured results faithfully uncover the parity properties of the disclination states, beside revealing their existence. Similarly, in pump-probe II, a peak (dip) is observed at 10.12 (10.26) kHz associated with the disclination state $\Psi_{\mathrm{II},E}$ ($\Psi_{\mathrm{II},O}$) of even (odd) parity. We further measure the acoustic wave functions of the disclination states at resonant excitation conditions. Figure 3(h) presents the measured acoustic pressure in the cavities around the disclination core for $\Psi_{\mathrm{I},O}$ and $\Psi_{\mathrm{II},E}$. The experimental data confirm the following features.: the group I (II) eigenstate $\Psi_{\mathrm{I},O}$ ($\Psi_{\mathrm{II},E}$) is localized mainly in the B-type (A-type) cavities around the disclination core. These observations are consistent with the simulation results in Figs. 3(b)–3(e). More data showing the in-plane p-orbital wave patterns and the simulations of the local curvature effect are presented in Supplemental Material [46].

For the hyperbolic lattice, we consider a structure with 200 acoustic cavities [Fig. 4(a)]. The hyperbolic lattice has an emergent S_4 rotation symmetry which is a feature of the non-Euclidean geometry. From simulation, four disclination states emerge in the band gap: Ψ_{E1} at 8.98 kHz, Ψ_{E2} at 9.28 kHz, and Ψ_{O1} and Ψ_{O2} at 9.12 kHz. Compared with the case of conic lattice, the four disclination states here are nearly degenerate and their wave functions all concentrate on the B-type cavities [Figs. 4(b)–4(e)]. Nevertheless, the wave functions show clear in-plane p-orbital wave patterns as well.

The 3D-printed acoustic hyperbolic lattice and two pump-probe configurations are shown in Fig. 4(f). For the bulk pump-probe configuration, both the source and the detector are away from the disclination core. For the disclination pump-probe configuration, the source and the detector are at the opposite sides of the disclination core. The measured acoustic responses for the two configurations are shown in Fig. 4(g). The bulk response has a suppressed region from 8.8 to 10.4 kHz due to the topological band gap. In contrast, the disclination response has a strong peak at 9.20 kHz due to the nearly degenerate disclination states. The detected acoustic wave pattern shows that the acoustic waves are indeed concentrated in the B-type cavities—a feature consistent with the simulation results in Figs. 4(b)–4(e). Moreover, the detected signals at D_1 and D_2 have nearly opposite amplitude in a broad frequency range [Fig. 4(h)]. This reveals that the acoustic wave switches sign in a cavity—an important feature of the in-plane p-orbital waves for the disclination states in Figs. 4(b)–4(e) (see Supplemental Material [46] for more results).

This study unveils the intriguing interplay between the band topology and the non-Euclidean geometries due to topological defects. Such interplay is further enriched by the p-orbital physics, leading to rich emergent p-wave behaviors for the bound modes as revealed by consistent experiments and simulations. Topological defects with finite Gaussian curvatures are common in nanostructures such as nanocones and nanorings [32,33] as well as in 2D materials [2–5,33–35,51,52], interfaces, and grain boundaries in crystals [43], which are yet to be explored for nontrivial topological phenomena of electrons and phonons. Using acoustic analogs, our study serves as a pioneering study into such a realm with nonplanar geometries and may inspire future studies on topological phenomena in nanomaterials and boundaries with curved surfaces as well as topological non-Euclidean metamaterials.

We acknowledge support from the National Natural Science Foundation of China (Grants No. 12104169, No. 92050102, No. 11874311, and No. 12074281), the Fundamental Research Funds for the Central Universities (Grant No. 20720200074) and the Huaqiao University (Grant No. 605-50Y21003). We also acknowledge the helpful discussions from Yixiao Ge.

*These authors contributed equally to this work.
†Corresponding author.
yingchen@hqu.edu.cn
‡Corresponding author.
jianhuajiang@suda.edu.cn
§Corresponding author.
kenyon@xmu.edu.cn

[1] M. Kleman and J. Friedel, Disclinations, dislocations, and continuous defects: A reappraisal, Rev. Mod. Phys. **80**, 61 (2008).
[2] J. K. Pachos, M. Stone, and K. Temme, Graphene with Geometrically Induced Vorticity, Phys. Rev. Lett. **100**, 156806 (2008).
[3] A. Cortijo and M. A. H. Vomediano, Effects of topological defects and local curvature on the electronic properties of planar graphene, Nucl. Phys. **B807**, 659 (2009).
[4] M. A. H. Vozmediano, M. I. Katsnelson, and F. Guinea, Gauge fields in graphene, Phys. Rep. **496**, 109 (2010).
[5] O. V. Yazyev and S. G. Louie, Topological defects in graphene: Dislocations and grain boundaries, Phys. Rev. B **81**, 195420 (2010).
[6] Y. Ran, Y. Zhang, and A. Vishwanath, One-dimensional topologically protected modes in topological insulators with lattice dislocations, Nat. Phys. **5**, 298 (2009).
[7] J. C. Y. Teo and C. L. Kane, Topological defects and gapless modes in insulators and superconductors, Phys. Rev. B **82**, 115120 (2010).
[8] V. Juricic, A. Mesaros, R. J. Slager, and J. Zaanen, Universal Probes of Two-Dimensional Topological Insulators: Dislocation and π Flux, Phys. Rev. Lett. **108**, 106403 (2012).
[9] A. Ruegg and C. Lin, Bound States of Conical Singularities in Graphene-Based Topological Insulators, Phys. Rev. Lett. **110**, 046401 (2013).
[10] F. de Juan, A. Ruegg, and D. H. Lee, Bulk-defect correspondence in particle-hole symmetric insulators and semimetals, Phys. Rev. B **89**, 161117(R) (2014).
[11] R. J. Slager, A. Mesaros, V. Juricic, and J. Zaanen, Interplay between electronic topology and crystal symmetry:

Dislocation-line modes in topological band insulators, Phys. Rev. B **90**, 241403(R) (2014).
[12] G. van Miert and C. Ortix, Dislocation charges reveal two-dimensional topological crystalline invariants, Phys. Rev. B **97**, 201111(R) (2018).
[13] R. Queiroz, I. C. Fulga, N. Avraham, H. Beidenkopf, and J. Cano, Partial Lattice defects in Higher-Order Topological Insulators, Phys. Rev. Lett. **123**, 266802 (2019).
[14] T. Li, P. Zhu, W. A. Benalcazar, and T. L. Hughes, Fractional disclination charge in two-dimensional C_n-symmetric topological crystalline insulators, Phys. Rev. B **101**, 115115 (2020).
[15] B. Roy and V. Juričić, Dislocation as a bulk probe of higher-order topological insulators, Phys. Rev. Res. **3**, 033107 (2021).
[16] H. Sumiyoshi and S. Fujimoto, Torsional Chiral Magnetic Effect in a Weyl Semimetal with a Topological Defect, Phys. Rev. Lett. **116**, 166601 (2016).
[17] M. N. Chernodub and M. A. Zubkov, Chiral anomaly in Dirac semimetals due to dislocations, Phys. Rev. B **95**, 115410 (2017).
[18] R. Soto-Garrido, E. Muñoz, and V. Juričić, Dislocation defect as a bulk probe of monopole charge of multi-Weyl semimetals, Phys. Rev. Res. **2**, 012043(R) (2020).
[19] J. Paulose, B. G. G. Chen, and V. Vitelli, Topological modes bound to dislocations in mechanical metamaterials, Nat. Phys. **11**, 153 (2015).
[20] F.-F. Li, H.-X. Wang, Z. Xiong, Q. Lou, P. Chen, R.-X. Wu, Y. Poo, J.-H. Jiang, and S. John, Topological light-trapping on a dislocation, Nat. Commun. **9**, 2462 (2018).
[21] A. K. Nayak, J. Reiner, R. Queiroz, H. X. Fu, C. Shekhar, B. H. Yan, C. Felser, N. Avraham, and H. Beidenkopf, Resolving the topological classification of bismuth with topological defects, Sci. Adv. **5**, eaax6996 (2019).
[22] Y. Liu, S. Leung, F.-F. Li, Z.-K. Lin, X. Tao, Y. Poo, and J.-H. Jiang, Bulk-disclination correspondence in topological crystalline insulators, Nature (London) **589**, 381 (2021).
[23] C. W. Peterson, T. Li, W. Jiang, T. L. Hughes, and G. Bahl, Trapped fractional charges at bulk defects in topological insulators, Nature (London) **589**, 376 (2021).
[24] H. Xue, D. Jia, Y. Ge, Y. Guan, Q. Wang, S. Yuan, H. Sun, Y. D. Chong, and B. Zhang, Observation of Dislocation-Induced Topological Modes in a Three-Dimensional Acoustic Topological Insulator, Phys. Rev. Lett. **127**, 214301 (2021).
[25] L. Ye, C. Qiu, M. Xiao, T. Li, J. Du, M. Ke, and Z. Liu, Topological dislocation modes in three-dimensional acoustic topological insulators, Nat. Commun. **13**, 508 (2022).
[26] Z.-K. Lin, Y. Wu, B. Jiang, Y. Liu, S. Wu, F. Li, and J.-H. Jiang, Topological Wannier cycles induced by sub-unit-cell artificial gauge flux in a sonic crystal, Nat. Mater. **21**, 430 (2022).
[27] S. S. Yamada, T. Li, M. Lin, C. W. Peterson, T. L. Hughes, and G. Bahl, Bound states at partial dislocation defects in multipole higher-order topological insulators, Nat. Commun. **13**, 1 (2022).
[28] Q. Wang, Y. Ge, H. X. Sun, H. Xue, D. Jia, Y. J. Guan, S. Q. Yuan, B. Zhang, and Y. D. Chong, Vortex states in an acoustic Weyl crystal with a topological lattice defect, Nat. Commun. **12**, 3654 (2021).
[29] Q. Wang, H. Xue, B. L. Zhang, and Y. D. Chong, Observation of Protected Photonic Edge States Induced by Real-Space Topological Lattice Defects, Phys. Rev. Lett. **124**, 243602 (2020).
[30] Y. Deng, W. A. Benalcazar, Z.-G. Chen, M. Oudich, G. Ma, and Y. Jing, Observation of Degenerate Zero-Energy Topological States at Disclinations in an Acoustic Lattice, Phys. Rev. Lett. **128**, 174301 (2022).
[31] Marco Miniaci, Florian Allein, and Raj Kumar Pal, Spectral flow of a localized mode in elastic media, arXiv:2111.09021.
[32] S. Gupta and A. Saxena, A topological twist on materials science, MRS Bull. **39**, 265 (2014).
[33] N. Karousis, I. Suarez-Martinez, C. P. Ewels, and N. Tagmatarchis, Structure, properties, functionalization, and applications of carbon nanohorns, Chem. Rev. **116**, 4850 (2016).
[34] S. Iijima, T. Ichihashi, and Y. Ando, Pentagons, heptagons and negative curvature in graphite microtubule growth, Nature (London) **356**, 776 (1992).
[35] P. E. Lammert and V. H. Crespi, Topological Phases in Graphitic Cones, Phys. Rev. Lett. **85**, 5190 (2000).
[36] Y. Tokura and N. Nagaosa, Orbital physics in transition-metal oxides, Science **288**, 462 (2000).
[37] C. Wu, Orbital Analogue of the Quantum Anomalous Hall Effect in p-Band Systems, Phys. Rev. Lett. **101**, 186807 (2008).
[38] G. Wirth, M. Ölschläger, and A. Hemmerich, Evidence for orbital superfluidity in the P-band of a bipartite optical square lattice, Nat. Phys. **7**, 147 (2011).
[39] P. Soltan-Panahi, D S. Lühmann, J. Struck, P. Windpassinger, and K. Sengstock, Quantum phase transition to unconventional multi-orbital superfluidity in optical lattices, Nat. Phys. **8**, 71 (2012).
[40] T. Jacqmin, I. Carusotto, I. Sagnes, M. Abbarchi, D. D. Solnyshkov, G. Malpuech, E. Galopin, A. Lemaître, J. Bloch, and A. Amo, Direct Observation of Dirac Cones and a Flatband in a Honeycomb Lattice for Polaritons, Phys. Rev. Lett. **112**, 116402 (2014).
[41] Guancong Ma, Meng Xiao, and C. T. Chan, Topological phases in acoustic and mechanical systems, Nat. Rev. Phys. **1**, 281 (2019).
[42] T. Kamada and S. Kawai, An algorithm for drawing general undirected graphs, Inf. Proc. Lett. **31**, 7 (1989). This is a force-directed graph algorithm that tends to find the optimal distances between nodes in n-dimensional ($n \geq 2$) space.
[43] W. T. M. Irvine, V. Vitelli, and P. M. Chaikin, Pleats in crystals on curved surfaces, Nature (London) **468**, 947 (2010).
[44] C. Wu and S. Das Sarma, $P_{x,y}$-orbital counterpart of graphene: Cold atoms in the honeycomb optical lattice, Phys. Rev. B **77**, 235107 (2008).
[45] X. Lu, Y. Chen, and H. Y. Chen, Orbital corner states on breathing kagome lattices, Phys. Rev. B **101**, 195143 (2020).
[46] See Supplemental Material at http://link.aps.org/supplemental/10.1103/PhysRevLett.129.154301 for more details of the contents of eigenmodes of coupled cavities, tight-binding calculations, topological invariants and Wannier centers, the effects of local curvature, topological corner states, and more experimental results.

[47] Jiuyang Lu, Chunyin Qiu, Manzhu Ke, and Zhengyou Liu, Valley Vortex States in Sonic Crystals, Phys. Rev. Lett. **116**, 093901 (2016).

[48] Jiuyang Lu, Chunyin Qiu, Liping Ye, Xiying Fan, Manzhu Ke, Fan Zhang, and Zhengyou Liu, Observation of topological valley transport of sound in sonic crystals, Nat. Phys. **13**, 369 (2017).

[49] W. A. Benalcazar, T. Li, and T. L. Hughes, Quantization of fractional corner charge in C_n-symmetric higher-order topological crystalline insulators, Phys. Rev. B **99**, 245151 (2019).

[50] H.-X. Wang, L. Liang, B. Jiang, J. Hu, X. Lu, and J.-H. Jiang, Higher-order topological phases in tunable C_3 symmetric photonic crystals, Photonics Res. **9**, 1854 (2021).

[51] C. Zhi, Y. Bando, C. Tang, and D. Golberg, Electronic structure of boron nitride cone-shaped nanostructures, Phys. Rev. B **72**, 245419 (2005).

[52] H. Ochoa, R. Zarzuela, and Y. Tserkovnyak, Emergent Gauge Fields from Curvature in Single Layers of Transition-Metal Dichalcogenides, Phys. Rev. Lett. **118**, 026801 (2017).